I&EC research
Industrial & Engineering Chemistry Research

pubs.acs.org/IECR
Article

Rational Design of Dual-Atom Catalysts for Electrochemical CO_2 Reduction to C_1 and C_2 Products with High Activity and Selectivity: A Density Functional Theory Study

Zhongze Bai, Zhuo Zhi, Xi Zhuo Jiang,* and Kai H. Luo*

Cite This: *Ind. Eng. Chem. Res.* 2025, 64, 4378−4387
Read Online

ABSTRACT: Carbon dioxide (CO_2) electroreduction using renewable energy provides a sustainable solution to mitigate greenhouse effects and achieve carbon neutrality. Developing high-performance electrocatalysts for the CO_2 reduction reaction (CO_2RR) is key to promoting such a technology. Herein, we systematically explored the CO_2RR catalytic activity of 325 dual-metal-site catalysts (DMSCs) through density functional theory (DFT) calculations. Among them, the Sc/Tc DMSC is particularly advantageous for HCOOH, CH_4, and CH_3CH_2OH production, with limiting potentials of −0.45 V, −0.45 V, and −0.46 V, respectively. The Ti/Rh DMSC can selectively convert CO_2 to CH_3CH_2OH at ultralow overpotentials (U_L = −0.21 V). HCOOH is the preferred product of the CO_2RR on the Mn/Fe site with a U_L of −0.30 V. Mn/Fe presents the highest inhibitory effects on the side reaction, the hydrogen evolution reaction (HER), with a U_L of −0.66 V. Moreover, electronic analysis was conducted to further explain the enhancement for the CO_2RR of explored catalysts at the subatomic level. Our work offers a strategy for screening of high-performance DMSCs and reveals the mechanisms of the CO_2RR to target products for selected catalysts, benefiting the further development of CO_2RR electrocatalysts.

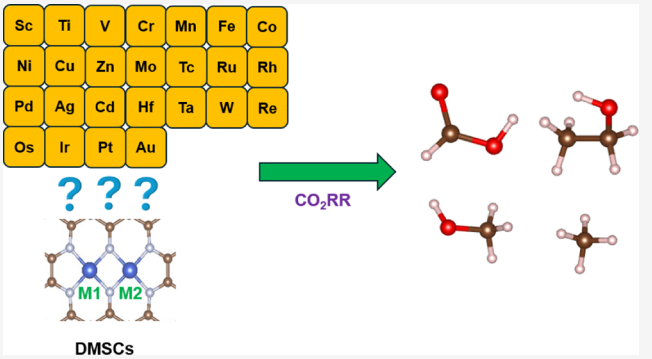

1. INTRODUCTION

The overuse of fossil energy has resulted in a significant rise in anthropogenic carbon dioxide (CO_2) concentration in the atmosphere, which is regarded as one of the primary drivers of global warming.[1−4] Thus, developing CO_2 utilization technologies is important and necessary to effectively address climate change and achieve carbon neutrality. The electrochemical CO_2 reduction reaction (CO_2RR) by clean renewable energy (sun, wind, etc.) is one of the promising technologies to convert CO_2 to chemicals.[5−10] However, the widespread deployment of the electrochemical CO_2RR is hindered by the unsatisfactory product selectivity, high overpotential, and sluggish kinetics of C_2 products with higher commercial value.[11−13] In the CO_2 electroreduction process, the CO_2 electroreduction performance is determined by electrocatalysts, and materials such as nonmetals,[14,15] nanostructured materials,[16−18] bulk metals, and alloys[19−21] have been identified as working electrocatalysts.

Recently, dual-metal-site catalysts (DMSCs) hold significant promise for the CO_2RR and have attracted a lot of research interest from both experiments and simulations. Li and co-workers discovered and synthesized Fe/Ni DMSC, which could promote the CO_2RR to CO with a U_L of −0.34 V.[22] Hao and co-workers found that the Ni/Ni DMSC had a promoting effect on the generation of CO during the CO_2RR with a Faradaic efficiency of over 99%.[23] Ag/Ag DMSC was prepared for the CO_2RR to CO by Li and co-workers by experiments.[24] They found that the Faradaic efficiency was up to 93.4% and the Ag/Ag catalyst had outstanding stability of more than 36 h.[24] Bai and co-workers chose the metal Cu, which has been proven to have the ability to reduce CO_2 to valuable hydrocarbons, as the candidate[25,26] and investigated the influence of the coordination environment on Cu-SACs and Cu-DACs by density functional theory (DFT) calculations.[27] The results showed that the CuCuNC-4a DMSC configuration could benefit C_2 product formation, but it suffered from aggressive competing reactions, hydrogen evolution reaction (HER), and the difficulty of CO_2 adsorption as well as C_2 product desorption. Thus, further improvement of the CO_2RR performance on DMSCs is of great importance and necessity. For DMSCs, the combinations of central metals and nonmetal coordination environments extend the possibility of designing high-performance catalysts for the electrochemical CO_2RR.

Received: December 18, 2024
Revised: February 4, 2025
Accepted: February 6, 2025
Published: February 18, 2025

https://doi.org/10.1021/acs.iecr.4c04831
Ind. Eng. Chem. Res. 2025, 64, 4378−4387

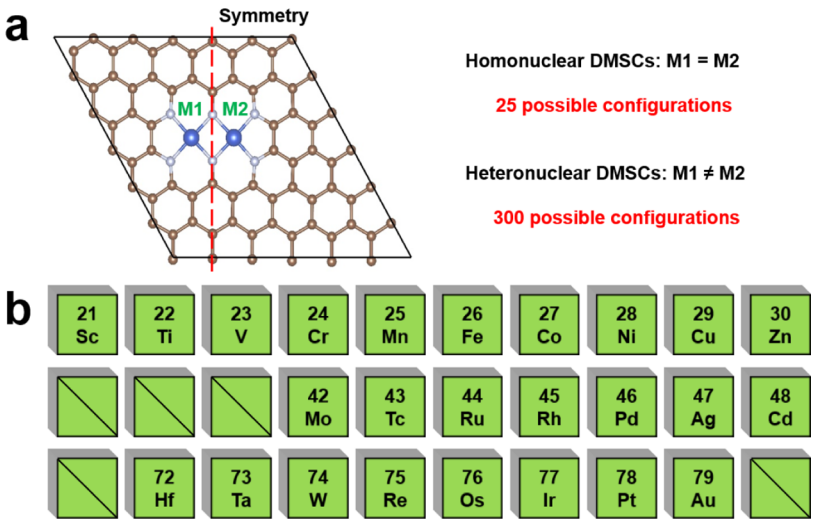

Figure 1. (a) Structures of DMSCs. (b) Screened transition metal elements.

High-throughput investigations of DMSCs could greatly contribute to the discovery of high-performance materials. For instance, Luo and co-workers designed Cu/Mn, Ni/Mn, and Ni/Fe DMACs for CO_2 conversion to CO via screening by DFT calculations.[28] Li and Tang enhanced the performance of CO generation during the CO_2RR on M2NC-4a DMSC by changing the central atoms.[29] Feng and co-workers successfully found four DMSCs for CO_2 electroreduction to CO through DFT calculations.[30] Ding and co-workers carried out DFT simulations to investigate the electrochemical CO_2RR to HCOOH and found five experimentally unexplored DMSCs that presented better CO_2RR abilities.[31] Chen and co-workers carried out computational screening for the reduction of CO_2 to C_2 products on M2NC−3 DMSCs with six possible transition metal atoms taken into account.[32] However, those studies mainly considered the adsorption of intermediates on metal atoms and neglected the adsorption of intermediates on surrounding atoms, which may lead to an inadequate evaluation of catalyst properties. Also, there is still a lack of systematic studies on how the central atom of the catalyst affects its behavior in the distribution of both C_1 and C_2 products during CO_2 electroreduction.

In this study, we systematically screen high-performance DMACs for the generation of both C_1 and C_2 chemicals (HCOOH, CH_3OH, CH_4, C_2H_6O, C_2H_4, and C_2H_6) during the electrochemical CO_2RR by DFT calculations. Based on a high-performance DMSC configuration[27] (Figure 1a), electrocatalysts containing elements from 25 transition metal elements (Sc, Ti, V, Cr, Mn, Fe, Co, Ni, Cu, Zn, Mo, Tc, Ru, Rh, Pd, Ag, Cd, Hf, Ta, W, Re, Os, Ir, Pt, and Au) (Figure 1b) are studied. The full description of the DMSC design and screening procedure is shown in Section 2.2.

2. METHODS

2.1. DFT Calculations. All spin-polarized DFT calculations were carried out using the Vienna Ab initio Simulation Package (VASP).[33,34] The exchange-correlation interactions were accounted for via the revised Perdew−Burke−Ernzerhof (RPBE) with the generalized gradient approximation (GGA).[35] The core electrons were treated by the projector augmented-wave (PAW) method.[36] The DFT-D3 method with Becke−Johnson damping was added to consider van der Waals interactions between atoms.[37,38] The Monkhorst−Pack k-point grids and cutoff energy were set to 3 × 3 × 1 and 500 eV, respectively. A 20 Å vacuum space was added along the Z-axis to reduce the interaction between adjacent layers. Convergence criteria of 0.02 eV/Å and 1.0×10^{-5} eV were set for the Hellmann−Feynman force and electronic energy, respectively. Implicit solvent models were implemented through the VASPsol code with ϵ_r of 78.4 to consider the electrolyte influence during the electrolytic process.[39−42] During the calculation of intermediate adsorption, we considered all adsorption sites involving both metal and nonmetal atoms and obtained their stable energies, selecting the structure with the lowest energy as the final stable configuration. The Gibbs free energy (ΔG) of intermediates throughout the CO_2 electroreduction process was calculated using the computational hydrogen electrode (CHE) model.[43,44] In the CHE model, the impact of the applied voltage (U) is accounted for by adjusting the free energy of the electrochemical reactions. Specifically, the free energy (ΔG) is corrected as:[43]

$$\Delta G(U) = \Delta G(0) - neU \quad (1)$$

where, $\Delta G(0)$ is the free energy under standard conditions, n is the number of electrons transferred, e is the elementary charge, and U is the applied potential.

The influence of pH is incorporated through the concentration of protons (H^+) involved in proton-coupled reactions. The free energy (ΔG) is corrected through eq 2:[43]

$$\Delta G(U) = \Delta G(0) + k_B T \ln(10) \times \mathrm{pH} \quad (2)$$

where, $\Delta G(0)$ is the free energy under standard conditions, k_B is the Boltzmann constant, and T represents temperature.

To calculate reaction barriers, the climbing image nudged elastic band (CI-NEB) approach was used to search for transition states (TS).[45] Moreover, VASPKIT[46] and QVASP[47] programs were used to aid in the computations. Crystal orbital Hamilton population (COHP) analysis was carried out through the local orbital basis suite toward electronic-structure reconstruction (LOBSTER).[48] All ab initio molecular dynamics (AIMD) computations were performed at 300 K for 10 ps using a Nose-Hoover thermostat with a time step of 1 fs. The data of the Cu/Cu DMSC are from our previous work.[27]

https://doi.org/10.1021/acs.iecr.4c04831
Ind. Eng. Chem. Res. 2025, 64, 4378−4387

The adsorption energy (E_{ads}) was calculated through eq 3:

$$E_{ads} = E_{M/C} - E_C - E_M \quad (3)$$

where $E_{M/C}$, E_C, and E_M denote the total energy of the catalyst and adsorbates, the energy of the catalyst, and the energy of adsorbates, respectively.

The Gibbs free energy (ΔG) change was calculated according to eq 4:[49]

$$\Delta G = \Delta E + \Delta E_{ZPE} - T\Delta S \quad (4)$$

where ΔE is the difference in electron energies obtained directly from DFT calculations. ΔE_{ZPE} and ΔS are the differences in zero-point energy and entropy between 0 K and room temperature (T = 298.15 K), respectively.

The limiting potential (U_L) was calculated by eq 5:[50−52]

$$U_L = -\Delta G_{max}/e \quad (5)$$

where ΔG_{max} represents the free energy difference between the potential limiting step (PLS) in CO_2RR at 0 V and the reversible hydrogen electrode (RHE).

To evaluate the thermodynamic stabilities of catalysts, the formation energy (E_f) was adopted and calculated as shown in eq 6:[53]

$$\Delta E_f = E_{Catalyst} + a\mu_C - (E_{gra} + b\mu_N + \mu_1 + \mu_2) \quad (6)$$

where $E_{Catalyst}$ and E_{gra} are the total energies of optimized catalysts and pristine graphene with 72 atoms, respectively. μ_N and μ_C are the energies of a nitrogen atom and a single carbon atom, respectively, which were calculated from graphene and isolated N_2 molecules. μ_1 and μ_2 are the energies of single metal atoms 1 and 2 in a vacuum, respectively. a is the number of C atoms that differ between catalysts and pure graphene. The number of N atoms in catalysts is denoted by b.

As shown in eqs 7 and 8,[54] the binding energy (E_{bin}) and cohesive energy (E_{coh}) were calculated to analyze the binding performance between the N-dropped graphene substrate and metal atoms.

$$E_{bin} = (E_{M/C} - E_{sub} - \mu_1 - \mu_2)/n \quad (7)$$

$$E_{coh} = E_{bulk} - m\mu \quad (8)$$

where n and m are the number of metal atoms in catalysts and bulk metals, respectively. μ is the single metal atom energy corresponding to the bulk metal.

Energy barrier (E_b) was calculated as presented in eq 9:

$$E_b = E(TS) - E(IS) \quad (9)$$

where E(TS) and E(IS) are the energies of the transition state and initial state, respectively.

2.2. DMSC Screening Procedure. In the DMSC structure, the two metals (M1 and M2) are equivalent sites. A total of 325 possible structures are considered, including 25 homonuclear (M1 = M2) and 300 heteronuclear (M1 ≠ M2) DMSCs. We first screened the stable DMSCs from all 325 possible structures. Second, catalysts with the adsorption energy of CO between −0.3 and 0.29 eV were selected. The competing HER reactions of DMSCs were inhibited by the selection of U_L (H_2) lower than −0.1 V. Also, we further screened catalysts with negative adsorption energy of CO_2, which could benefit the activation of CO_2 and facilitate the subsequent electrocatalytic reactions. After that, we screened catalysts with adsorption energies of the main C_1 and C_2 products higher than −0.1 eV to facilitate the desorption of generated products. Then, we revealed generation mechanisms of target products on DMSCs that satisfy the above conditions and selected catalysts with U_L of generated chemicals higher than U_L (H_2). At last, AIMD simulations at 300 K were carried out to examine the kinetic stabilities of screened catalysts. For C_2 chemicals, considering C−C coupling is a nonelectroreduction process, the energy barrier of C−C coupling was used as an indicator to determine whether the C_2 products are readily generated. In detail, catalysts with the energy barrier of C−C coupling less than 0.75 eV could benefit C_2 product formation, which is widely accepted by previous studies.[32,55] The screening process of the catalysts is illustrated in Figure 2. More details of the screening criteria are presented in Section 3.

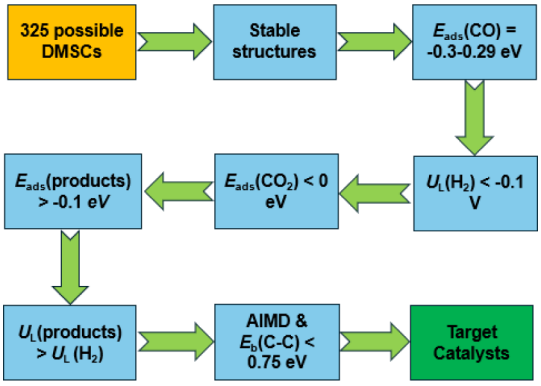

Figure 2. Schematic diagrams for screening DMSCs through the DFT method.

3. RESULTS

3.1. Identification of DMSCs with High Potential for CO_2 Reduction. The objective of this part is to identify high-potential DMSCs for further mechanism studies with stable configurations, as well as suitable E_{ads}(CO), U_L(H_2), E_{ads}(CO_2), and E_{ads}(products) values.

According to a previous study,[53] formation energies E_f and the difference between the binding and cohesive energies E_{b-c} ($E_{b-c} = E_{bin} - E_{coh}$) are adopted to evaluate the stability of DMACs. For stable configurations, the values of E_f and E_{b-c} are negative, indicating that catalysts are thermodynamically stable and metal atoms prefer to spread atomically on the graphene rather than aggregate into nanoparticles due to the coordination effect.[27,53] The objective of this section is to screen out stable DMSCs from the 325 possible configurations by E_f and E_{b-c}. The possible combinations of central metals and calculated E_f and E_{b-c} values are shown in Table S1, and 295 stable configurations are found, as shown in Table S2.

CO is a key intermediate for the generation of C_1 and C_2 chemicals during the electrochemical CO_2RR,[56] and thus the adsorption energy of CO, E_{ads}(CO), is an important indicator for the screening of DMSCs.[57,58] A weak CO adsorption indicates that CO is more likely to desorb from the catalyst, forming CO as the final product. Strong CO adsorption will inhibit subsequent reactions, generating valuable feedstocks. Thus, selecting catalysts with moderate E_{ads}(CO) is important and necessary for the discovery of DMSCs generating hydrocarbons. According to previous studies,[27,59] the CO adsorption energy of the Cu/Cu DMSC is 0.29 eV; lowering the CO adsorption energy is favorable for the generation of

https://doi.org/10.1021/acs.iecr.4c04831
Ind. Eng. Chem. Res. 2025, 64, 4378−4387

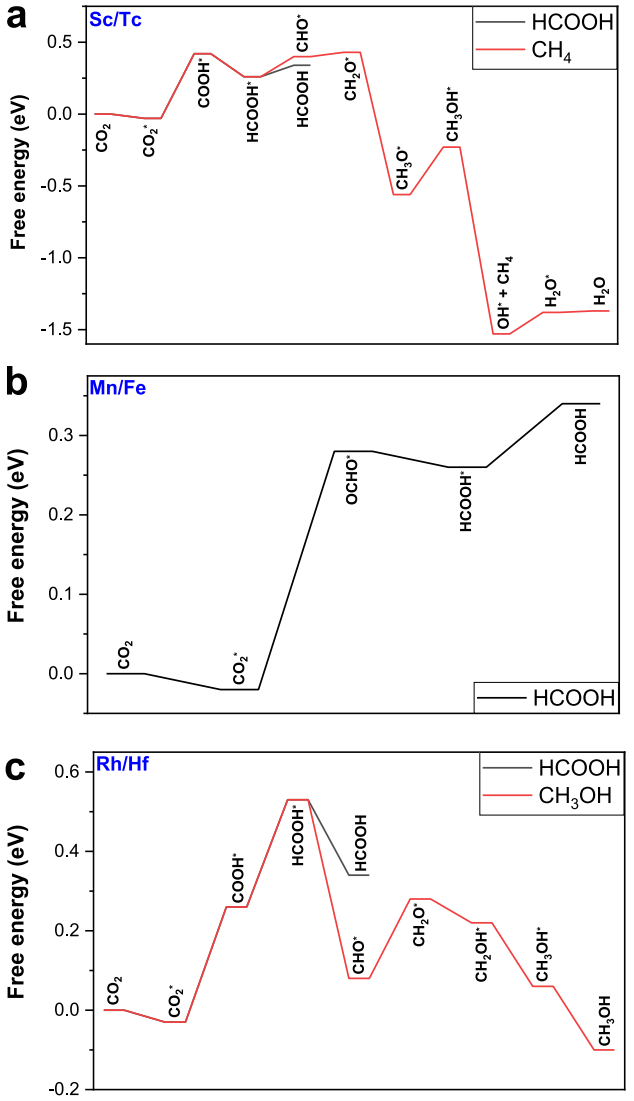

Figure 3. Most favorable reaction pathways of CO_2 electroreduction to C_1 chemicals on (a) Sc/Tc, (b) Mn/Fe, and (c) Rh/Hf at 0 applied voltage (symbol * represents the adsorbed state of intermediates).

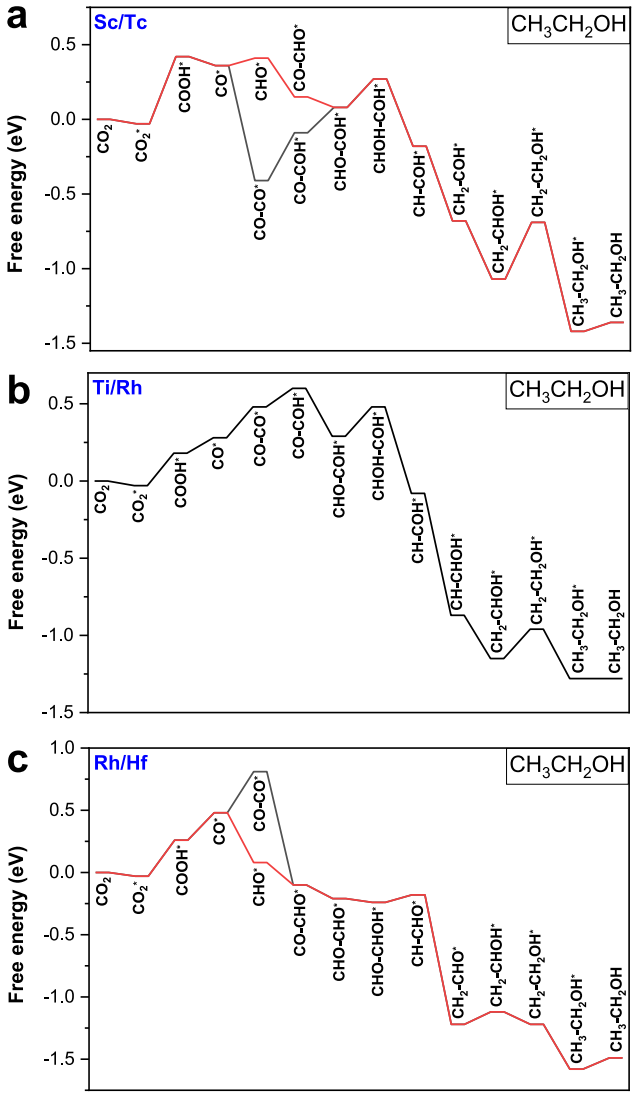

Figure 4. Most favorable reaction pathways of CO_2 electroreduction to CH_3CH_2OH on (a) Sc/Tc, (b) Ti/Rh, and (c) Rh/Hf at 0 applied voltage (symbol * represents the adsorbed state of intermediates).

valuable C_1 and C_2, however, this value should not be lower than −0.3 eV. The $E_{ads}(CO)$ values of 295 stable configurations are listed in Table S3, and 46 DMSCs are screened out as shown in Table S4.

During the electrochemical CO_2RR, the HER is the main competitive reaction. In our previous work, we found that the Cu/Cu DMSC suffered from aggressive competing reactions for H_2 formation with $U_L(H_2)$ of only −0.1 V.[27] To mitigate this problem, we screened out catalysts with $U_L(H_2)$ values lower than −0.1 V. The $U_L(H_2)$ values of 46 DMSCs are presented in Table S5. The 37 screened-out catalysts are described in Table S6.

Besides, the adsorption and activation of CO_2 on the catalyst surface are another obstacle for the CO_2RR as linear CO_2 molecules are stable and chemically inert with low electron affinity and a large energy gap.[8,60] The catalysts with negative adsorption energy of CO_2 are selected to promote this process.[61] The calculated $E_{ads}(CO_2)$ values are shown in Table S7, and 19 DMSCs are found with negative $E_{ads}(CO_2)$ as shown in Table S8.

The desorption of products from catalysts to release the active sites is also an important process affecting the performance of DMSCs. The strong adsorption of products will inhibit the release of target chemicals, and we selected catalysts with adsorption energies of target products above −0.1 eV to ensure that the products could easily detach from the catalyst.[59] During the CO_2 electroreduction process, HCOOH, CH_3OH, and CH_4 are the key C_1 chemicals, while C_2H_4, C_2H_6, and CH_3CH_2OH are the main C_2 products. According to the possible generation mechanisms of target products in our previous work,[27] the adsorption energies of HCOOH, CH_3OH, H_2O&CH_4, C_2H_4, C_2H_6, and C_2H_6O are used to reflect the generation abilities of HCOOH, CH_3OH, CH_4 C_2H_4, C_2H_6, and C_2H_6O, respectively. Table S9 shows the adsorption energies of the main products on 19 selected DMSCs. Overall, we identified a number of catalysts that would favor the generation of HCOOH, CH_3OH, CH_4, and C_2H_6O. Specifically, Sc/Tc, Sc/Rh, Mn/Fe, Mn/Cd, and Rh/Hf DMSCs can benefit HCOOH formation. Sc/Rh, Mn/Cd,

https://doi.org/10.1021/acs.iecr.4c04831
Ind. Eng. Chem. Res. 2025, 64, 4378−4387

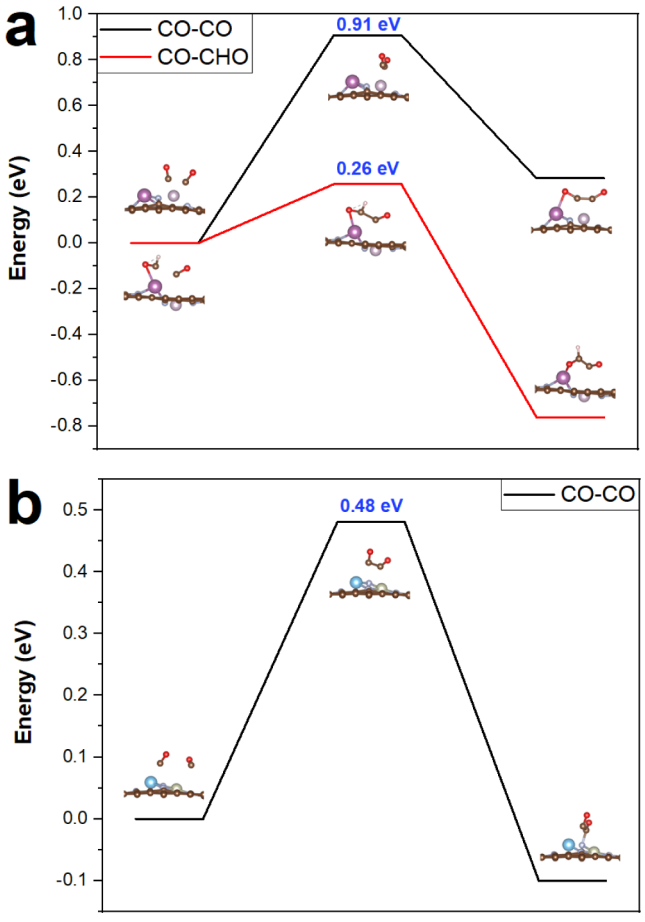

Figure 5. Coupling process of CO−CO*/CO−CHO* on the two possible DMSCs. (a) CO-CO* and CO−CHO* coupling on Sc/Tc, and (b) CO−CO* coupling on Ti/Rh.

and Rh/Hf DMSCs are favorable for the generation of CH_3OH. All catalysts except Cu/Pd, Cu/Pt, Pd/Pd, Pd/Pt, and Pt/Pt DMSCs have the potential to promote the formation of CH_4. Sc/Tc, Sc/Rh, Ti/Cu, Ti/Zn, Ti/Rh, Ti/Hf, Ti/W, Mn/Cd, and Rh/Hf DMSCs favor the C_2H_6O desorption.

3.2. CO_2RR Mechanisms and Identification of DMSCs through U_L(products). After the screening process described above, a total of 16 DMSCs with high potential for C_1 and C_2 chemical generation were selected from a total of 325 possible configurations. In this section, we reveal their CO_2RR mechanisms and calculate their limiting potential for product formation. The possible pathways for C_1 and C_2 chemical formation are shown in Figure S1, which refers to earlier studies.[27,62−64] It should be noted that we only considered the

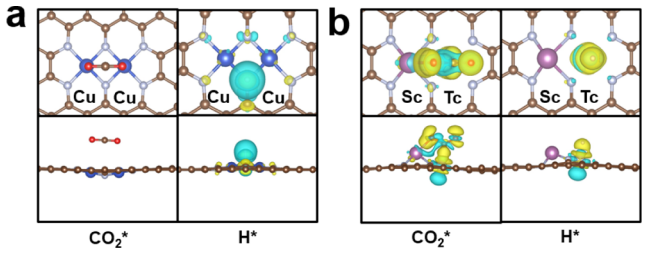

Figure 6. Charge density difference (CDD) of adsorbed CO_2 and H on the (a) Cu/Cu DMSC and (b) Rh/Hf DMSC. The isosurface value is 0.004 e/bohr^3. Yellow and blue regions denote charge accumulation and depletion, respectively.

potential pathways for C_2H_6O generation for C_2 compounds, as all screened DMSCs were in favor of the formation of C_2H_6O. The most favorable reaction pathways with the highest U_L values are chosen from the reaction network, and the DMSCs with U_L(products) higher than $U_L(H_2)$ are screened out for further investigation. After calculating all possible channels for the selected 16 DMSCs, we found that the Sc/Tc DMSC could benefit the generation of HCOOH, CH_4, and C_2H_6O. The Ti/Rh DMSC was screened out for C_2H_6O formation. The Mn/Fe DMSC showed good electroreduction catalytic performance on HCOOH generation. The Rh/Hf site was favorable for the formation of HCOOH, CH_3OH, and C_2H_6O during the CO_2RR. The detailed parameters of the screening process are provided in Table S10. Here, we listed the limiting potentials of the screened DMSCs during the CO_2RR to target products as well as the Gibbs free energy changes above H_2 generation during the generation of the products for the discarded catalysts.

3.2.1. CO_2RR Mechanisms to C_1 Chemicals. Figure 3 shows the reaction pathways of electroreduction of CO_2 to C_1 chemicals on the Sc/Tc DMSC, Mn/Fe DMSC, and Rh/Hf DMSC. The free energies of elementary steps are listed in Tables S11−S13, respectively. The optimized intermediates for CO_2 electroreduction on Sc/Tc, Mn/Fe and Rh/Hf sites are presented in Figures S2−S4, respectively. According to Figure 3a, the Sc/Tc DMSC benefits the formation of both HCOOH and CH_4 via the pathways $CO_2 \rightarrow CO_2^* \rightarrow COOH^* \rightarrow HCOOH^* \rightarrow HCOOH$ and $CO_2 \rightarrow CO_2^* \rightarrow COOH^* \rightarrow HCOOH^* \rightarrow CHO^* \rightarrow CH_2O^* \rightarrow CH_3O^* \rightarrow CH_3OH^* \rightarrow OH^* \rightarrow H_2O^* \rightarrow H_2O$, respectively. As shown in Figure 3b,c, the pathway for HCOOH formation on the Mn/Fe site is $CO_2 \rightarrow CO_2^* \rightarrow OCHO^* \rightarrow HCOOH^* \rightarrow HCOOH$. For the Rh/Hf DMSC, the channel is $CO_2 \rightarrow CO_2^* \rightarrow OCHO^* \rightarrow HCOOH^* \rightarrow HCOOH$. The pathway toward CH_3OH on the Rh/Hf DMSC is $CO_2 \rightarrow CO_2^* \rightarrow COOH^* \rightarrow HCOOH^* \rightarrow CHO^* \rightarrow CH_2O^* \rightarrow CH_2OH^* \rightarrow CH_3OH^* \rightarrow CH_3OH$.

Table 1. Summary of U_L and E_{ads} of the Main Chemicals during the CO_2RR on Cu/Cu, Sc/Tc, Ti/Rh, Mn/Fe, and Rh/Hf DMSCs[a]

U_L (V)	Cu/Cu	Sc/Tc	Ti/Rh	Mn/Fe	E_{ads} (eV)	Cu/Cu	Sc/Tc	Ti/Rh	Mn/Fe
H_2	−0.10	−0.66	−0.43	−0.47	CO_2	0.18	−0.03	−0.03	−0.02
HCOOH	−0.10	−0.45		−0.30	HCOOH	0.03	−0.08		−0.08
CH_3OH	−0.51				CH_3OH	−0.05			
CH_4	−0.51	−0.45			CH_4	0.23	0.00		
C_2H_6O	−0.36	−0.46	−0.21		C_2H_6O	−0.19	0.01	0.00	

[a]The data for the Cu/Cu DMSC are reproduced from ref 27 available under a CC-BY 3.0 license. Copyright 2023 Bai, Z.; Jiang, X. Z.; and Luo, K. H.

https://doi.org/10.1021/acs.iecr.4c04831
Ind. Eng. Chem. Res. 2025, 64, 4378−4387

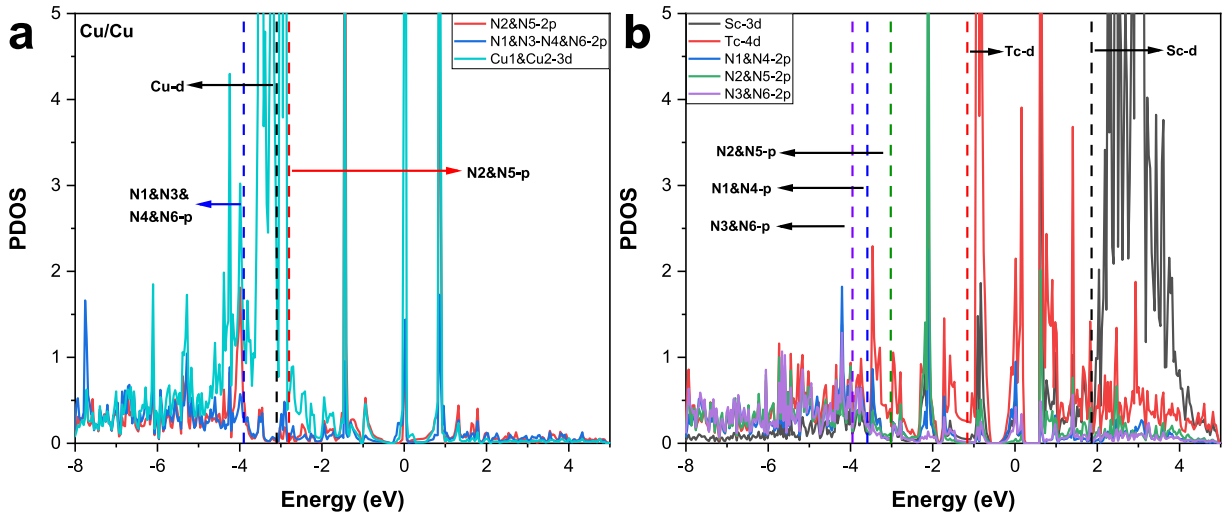

Figure 7. Partial density of states (PDOS) analysis of the (a) Cu/Cu DMSC (reproduced from ref 27, available under a CC-BY 3.0 license. Copyright 2023, Bai, Z.; Jiang, X. Z.; and Luo, K. H) and (b) Sc/Tc DMSC. The dotted lines in the diagram represent the bond centers of atoms.

CO_2* → COOH* is the common limiting step for the CO_2RR on Sc/Tc and Rh/Hf DMSCs with U_L of −0.45 V and −0.29 V, respectively. For the Mn/Fe site, the conversion of CO_2* to OCOH* is the limiting step for the conversion of the CO_2RR to HCOOH with a U_L of −0.30 V.

3.2.2. CO_2RR Mechanisms to C_2 Chemicals. According to previous studies,[42,65] CO*−CO*, CO*-CHO*, and CO*-COH* are three main pathways for C−C coupling, which is the key step for C_2 chemical generation. Among them, CO*-COH* is not considered in the current work as the formation of COH* via CO* → COH* is difficult, with relatively high free energy changes of 1.49, 1.56, and 1.47 eV on Sc/Tc, Ti/Rh, and Rh/Hf DMSCs, respectively. Figure 4 shows the most favorable reaction pathways with the lowest limiting potential of CO_2 electroreduction to CH_3CH_2OH on target DMSCs. The channels for the CO_2RR to CH_3CH_2OH on Sc/Tc, Ti/Rh, and Rh/Hf DMSCs are CO_2 → CO_2* → COOH* → CO* → CO−CO*/CHO* → CO−COH*/CO−CHO* → CHO−COH* → CHOH−COH* → CH−COH* → CH_2−COH* → CH_2−CHOH* → CH_2−CH_2OH* → CH_3−CH_2OH*, CO_2 → CO_2* → COOH* → CO* → CO−CO* → CO−COH* → CHO−COH* → CHOH−COH* → CH−COH* → CH−CHOH* → CH_2−CHOH* → CH_2−CH_2OH* → CH_3−CH_2OH* → CH_3−CH_2OH and CO_2 → CO_2* → COOH* → CO* → CO−CO*/CHO* → CO−CHO* → CHO−CHO* → CHO−CHOH* → CH−CHO* → CH_2−CHO* → CH_2−CHOH* → CH_2−CH_2OH* → CH_3−CH_2OH* → CH_3−CH_2OH, respectively. Figures S5−S7 present the optimized intermediates for the CO_2RR on Sc/Tc, Ti/Rh, and Rh/Hf DMSCs. The relevant free energies of elementary steps are presented in Tables S14−S16, respectively. The limiting step for CH_3CH_2OH formation on the Sc/Tc site is CHOH−COH* → CH−COH* with a U_L of −0.46 V. The U_L for CH_3CH_2OH generation on the Ti/Rh DMSC is −0.21 V via channel CO* to COOH*. CO_2* → COOH* is the limiting step for the CO_2RR toward CH_3CH_2OH on the Rh/Hf DMSC with a U_L of −0.29 V.

3.3. Kinetic Stability Analysis. To discuss the kinetic stability of the four discovered DMSCs, 10 ps AIMD simulations at 300 K are carried out for Sc/Tc, Ti/Rh, and Mn/Fe DMSCs. For the Rh/Hf site, only 2.44 ps AIMD simulations are carried out, as the Hf atom has detached from the catalyst at the moment, which indicates that this configuration is dynamically unstable and therefore is screened out. Figure S8 presents the geometric structures before and after the AIMD simulations. Although Sc/Tc, Ti/Rh, and Mn/Fe DACs show some changes after AIMD simulations, there is still strong binding between the two metal atoms and their surrounding N atoms, and no evident structural deformation has been identified. Thus, these three potential DACs have a high degree of kinetic stability.

3.4. C−C Coupling Process and Performance Comparison of Discovered DMSCs. According to previous studies, the C−C coupling is a nonelectrochemical process and the energy barrier (E_b) is the important factor in determining whether the C−C bond can form.[32,66,67] The C−C coupling process on Sc/Tc and Ti/Rh DMSCs is shown in Figure 5. By comparing the threshold value of E_b of 0.75 eV,[32,55] the CO−CHO* on Sc/Tc and CO−CO* coupling on Ti/Rh are easy to happen with E_b of 0.26 and 0.48 eV, respectively. However, the CO−CO coupling on Sc/Tc suffers from a high E_b of 0.91 eV (higher than 0.75 eV). C−C bond formation on the Sc/Tc DMSC is more favored through CO−CHO coupling with the pathway of CH_3CH_2OH formation of CO_2 → CO_2* → COOH* → CO* → CHO* → CO−CHO* → CHO−COH* → CHOH−COH* → CH−COH* → CH_2−COH* → CH_2−CHOH* → CH_2−CH_2OH* → CH_3−CH_2OH* → CH_3−CH_2OH.

To better clarify the performance of the discovered catalysts, we compared the U_L and E_{ads} of the main chemicals during the CO_2RR on Cu/Cu, Sc/Tc, Ti/Rh, and Mn/Fe DMSCs, as shown in Table 1. Compared with the Cu/Cu DMSC, all three discovered DMSCs present strong inhibitory and promotional effects on H_2 production and CO_2 adsorption, respectively. Among them, the Sc/Tc DMSC has the most pronounced inhibition of H_2 with its U_L as low as −0.66 V. There was no significant difference in the promotion of CO_2 adsorption among the four DMSCs. They all have higher product selectivity than the Cu/Cu DMSC with U_L (products) less than U_L (H_2). The Ti/Rh DMSC requires the lowest external voltage with U_L (products) of only −0.21 V and consumes the least amount of energy to generate the product in the electrocatalytic process. Regarding product desorption, Sc/Tc

https://doi.org/10.1021/acs.iecr.4c04831
Ind. Eng. Chem. Res. 2025, 64, 4378−4387

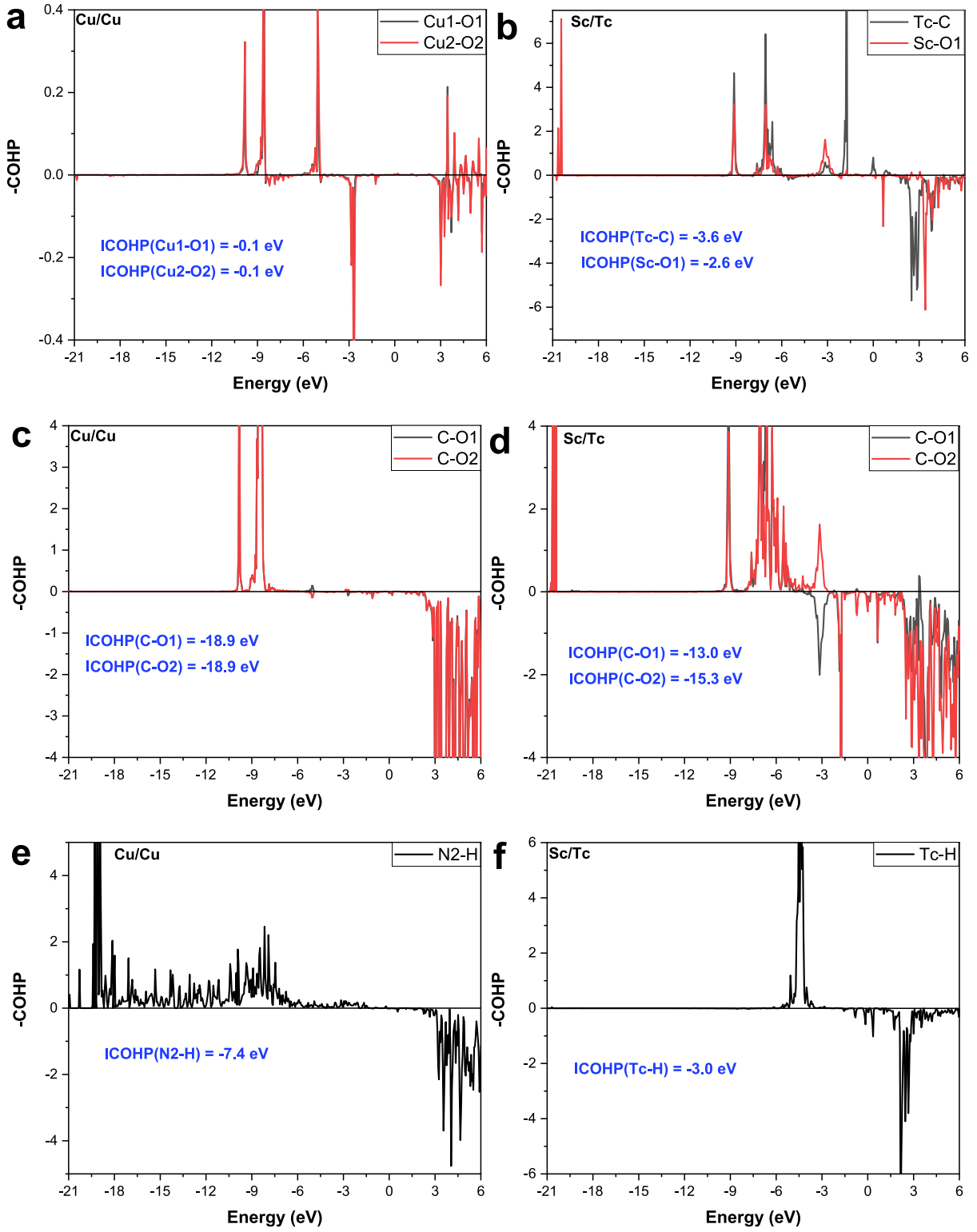

Figure 8. Crystal orbital Hamilton population (COHP) between Cu1−O1 and Cu2−O2 on (a) the Cu/Cu DMSC, Tc−C and ScO1 on (b) the Sc/Tc DMSC, C−O1 and C−O2 on (c) the Cu/Cu DMSC, C−O1 and C−O2 on (d) the Sc/Tc DMSC, N2−H on (e) the Cu/Cu DMSC, and (f) Tc−H on the Sc/Tc DMSC.

and Ti/Rh DMSCs greatly improve C_2H_6O desorption compared to the Cu/Cu site.

3.5. Electronic Analysis. Based on the above analysis, the CO_2RR performance of DMSCs is significantly enhanced by altering the central metal atoms, specifically inhibiting H_2 generation as well as promoting CO_2 adsorption. To further clarify the enhancement of the CO_2RR for the explored catalysts, the Sc/Tc DMSC is selected as the representative that has the lowest U_L (CO_2) and U_L (H_2) among explored catalysts for electronic analysis through charge density

https://doi.org/10.1021/acs.iecr.4c04831
Ind. Eng. Chem. Res. 2025, 64, 4378−4387

difference (CDD), partial density of states (PDOS) and crystal orbital Hamilton population (COHP) analysis.

Figure 6a,b present the CDD of adsorbed CO_2 and H on Cu/Cu and Sc/Tc DMSCs, respectively. The position numbers of C, N, O, as well as H and central metal atoms are shown in Figure S9, and the relevant Bader charges are listed in Table S16. There was no significant charge transfer during the adsorption of CO_2 on the Cu/Cu DMSC, with a total charge transfer of only 0.02 electrons. For the Sc/Tc catalyst, electrons transfer from the catalyst to CO_2 during the adsorption process, with a 0.90 charge change through Tc−C and Sc−O1 bonds. CO_2 adsorbs onto catalyst Sc/Tc with significantly more charge transfer than the Cu/Cu DMSC, indicating that the Sc/Tc site adsorbs CO_2 more strongly than the Cu/Cu DMSC and thus has a lower adsorption energy. For the H atom, H adsorbs to the Cu/Cu site by generating the N2−H bond with the N2 atom, and 0.48 electrons are transferred from the H atom to the N2 atom. However, H forms a Tc−H bond with the Tc atom on the Sc/Tc DMSC, with 0.20 electrons (less than that of the Cu/Cu DMSC) transferring from the Tc atom to the H atom. The bond length of Tc−C (1.62 Å) is longer than that of N2−C (1.02 Å), indicating the Cu/Cu site adsorbs H more strongly than the Sc/Tc DMSC, with adsorption energies of −0.10 and 0.66 eV, respectively.

Figure 7a,b display the partial density of states (PDOS) results of Cu/Cu and Sc/Tc DMSCs. Bond centers of relevant atoms are listed in Table S17. For the Cu/Cu site, PDOS values of N1, N3, N4, and N6 are the same, and the 2p bond center is −3.9 eV. The Cu-3d bond center is −3.1 eV, and the 2p bond centers of both N2 and N5 are −2.8 eV. Among them, the 2p bond center of N2 and N5 is the closest to the Fermi energy level (0 eV), which means N2 and N5 sites have a stronger interaction with intermediates. This agrees well with the adsorption sites for H and other important carbon-containing intermediates on the Cu/Cu DMSC according to our previous research.[27] However, the reason why the sites of CO_2 adsorption are not on N2 and N5 atoms could be due to the strong attraction of N atoms to charge and CO_2 will lose electrons in the adsorption process, which is the opposite of CO_2 adsorption and bending activation (getting electrons). The poor stability of the CO_2 intermediate after losing electrons makes the system relatively unstable. Thus, the active site for the most stable adsorption of CO_2 changes from N2 and N5 to Cu1 and Cu2, where CO_2 is more accessible to electrons. Regarding the Sc/Tc DMSC, the bond centers of Sc-3d and Tc-4d are 1.9 eV and −1.2 eV, respectively. The 2p bond centers of N1&N4, N2&N5, and N3&N6 are −3.6 eV, −3.0 eV, and −4.0 eV, respectively. As Tc-4d's bond center is the closest to the Fermi energy level among those atoms, Tc has a stronger interaction with intermediates, which is consistent with the observation in Figure 6b that CO_2 and H are adsorbed on the Tc atom of Sc/Tc DMSC.

COHP calculations are carried out during CO_2 and H adsorption on Cu/Cu and Sc/Tc catalysts for quantitative evaluation of the strength of different chemical bonds, as shown in Figure 8. During CO_2 adsorption onto the Cu/Cu DMSC, the −CHOPs of Cu1−O1&Cu2−O2 (Figure 8a) and C−O1&C−O2 (Figure 8c) bonds are the same, with integrated COHP (ICOHP) values of −0.1 eV and −18.9 eV, respectively. For CO_2 adsorption on the Sc/Tc site, the ICOHP values of Tc−C and Sc−O1 bonds are −3.6 eV and −2.6 eV (Figure 8b), which are lower than those of Cu1−O1 and Cu2−O2, corresponding to lower CO_2 adsorption energy, again demonstrating the stronger adsorption abilities of Sc/Tc to CO_2. The values of ICOHP for C−O1 and C−O2 are −13.0 eV and −15.3 eV (Figure 8d), respectively, which are higher than those of C−O1&C−O2. This implies that CO_2 adsorbs on Sc/Tc with lower C−O bond energies, and Sc/Tc promotes CO_2 activation, which also proves that low CO_2 adsorption energies facilitate CO_2 activation for subsequent reactions. Regarding H adsorption, according to Figure 8e,f, the ICOHP values of N2−H and Tc−H are −7.4 eV and −3.0 eV, respectively. Due to the lower ICOHP value for the Tc−H bond, the adsorption energy of H on the Sc/Tc catalyst will be higher, which in turn inhibits the H_2 generation reaction.

4. CONCLUSIONS

In the present study, we systematically explore the catalytic activity and selectivity of dual-metal-site catalysts (DMSCs) considering all of the central metals and the environmental nonmetals through DFT calculations. Considering stabilities, adsorption energy of CO, limiting potential of H_2, adsorption energy of CO_2, energy change of CO−CO, adsorption energy of main chemicals, limiting potential of target products and energy barriers of the C−C coupling process, three novel high-performance DMSCs with high activity and selectivity for product formation during the CO_2RR from 325 possible structures are discovered. Specifically, the Sc/Tc DMSC is favorable for HCOOH, CH_4, and CH_3CH_2OH formation with limiting potentials of −0.45 V, −0.45 V, and −0.46 V, respectively. The Ti/Rh DMSC can selectively reduce CO_2 to CH_3CH_2OH with ultralow overpotentials (U_L = −0.21 V). HCOOH is the target product for the Mn/Fe site with a U_L of −0.30 V. Mn/Fe has the most significant inhibitory performance on the HER among those catalysts with a U_L of −0.66 V. Our study sheds light on the CO_2RR mechanism of DMSCs and proves that constructing heteronuclear dual-atom active sites is an effective method to develop high-performance electrocatalysts. Finally, we establish a systematic procedure to explore outstanding catalysts for the CO_2RR. Future work could involve experimental validation and the industrial application of the high-performance catalysts identified in this study. Additionally, exploring the integration of DFT with machine learning could further reduce computational costs and accelerate the design of new catalysts.

■ ASSOCIATED CONTENT

Supporting Information

The Supporting Information is available free of charge at https://pubs.acs.org/doi/10.1021/acs.iecr.4c04831.

CO_2RR pathways (Figure S1); optimized substrate and intermediate structures (Figures S2−S7); AIMD simulations (Figure S8); atomic number (Figure S9); catalyst composition during screening (Tables S1−S10); free energy for elementary steps (Tables S11−S16); bond center analysis (Table S17) (PDF)

■ AUTHOR INFORMATION

Corresponding Authors

Xi Zhuo Jiang − *School of Mechanical Engineering and Automation, Northeastern University, Shenyang, Liaoning 110819, PR China*; Email: jiangxz@mail.neu.edu.cn

Kai H. Luo − *Department of Mechanical Engineering, University College London, London WC1E 7JE, U.K.;*

https://doi.org/10.1021/acs.iecr.4c04831
Ind. Eng. Chem. Res. 2025, 64, 4378−4387

orcid.org/0000-0003-4023-7259; Email: k.luo@ucl.ac.uk

Authors

Zhongze Bai − *Department of Mechanical Engineering, University College London, London WC1E 7JE, U.K.*

Zhuo Zhi − *Department of Electronic and Electrical Engineering, University College London, London WC1E 7JE, U.K.*

Complete contact information is available at: https://pubs.acs.org/10.1021/acs.iecr.4c04831

Notes

The authors declare no competing financial interest.

■ ACKNOWLEDGMENTS

Support from the UK Engineering and Physical Sciences Research Council under Grant Nos. EP/T015233/1 and EP/X035875/1 is gratefully acknowledged. This work made use of computational support by CoSeC, the Computational Science Centre for Research Communities, through UKCOMES.

■ REFERENCES

(1) Wang, G.; Chen, J.; Ding, Y.; Cai, P.; Yi, L.; Li, Y.; Tu, C.; Hou, Y.; Wen, Z.; Dai, L. Electrocatalysis for CO_2 conversion: From fundamentals to value-added products. *Chem. Soc. Rev.* **2021**, *50* (8), 4993−5061.

(2) Goeppert, A.; Czaun, M.; Jones, J.-P.; Prakash, G. K. S.; Olah, G. A. Recycling of carbon dioxide to methanol and derived products − closing the loop. *Chem. Soc. Rev.* **2014**, *43* (23), 7995−8048.

(3) Bai, Z.; Jiang, X. Z.; Luo, K. H. Effects of Electric Field on Chemical Looping Combustion: A DFT Study of CO Oxidation on CuO (111) Surface. *ACS Omega* **2024**, *9* (19), 21082−21088.

(4) Jung, H. D.; Back, S. Theoretical study of CO2 electroreduction to C_3+ liquid chemicals. *Chem. Catal.* **2023**, *3* (12), 100845.

(5) Lees, E. W.; Mowbray, B. A.; Parlane, F. G.; Berlinguette, C. P. Gas diffusion electrodes and membranes for CO_2 reduction electrolysers. *Nat. Rev. Mater.* **2022**, *7* (1), 55−64.

(6) Gao, D.; Zhang, Y.; Zhou, Z.; Cai, F.; Zhao, X.; Huang, W.; Li, Y.; Zhu, J.; Liu, P.; Yang, F.; Wang, G. Enhancing CO_2 Electroreduction with the Metal−Oxide Interface. *J. Am. Chem. Soc.* **2017**, *139* (16), 5652−5655.

(7) Lee, J. H.; Kattel, S.; Xie, Z.; Tackett, B. M.; Wang, J.; Liu, C.-J.; Chen, J. G. Understanding the role of functional groups in polymeric binder for electrochemical carbon dioxide reduction on gold nanoparticles. *Adv. Funct. Mater.* **2018**, *28* (45), 1804762.

(8) Fu, L.; Wang, R.; Zhao, C.; Huo, J.; He, C.; Kim, K.-H.; Zhang, W. Construction of Cr-embedded graphyne electrocatalyst for highly selective reduction of CO_2 to CH_4: A DFT study. *Chem. Eng. J.* **2021**, *414*, 128857.

(9) Zhu, C.; Wu, G.; Mao, J.; Chen, A.; Zhao, Y.; Feng, G.; Wei, Y.; Liu, X.; Li, S.; Li, G.; Dong, X. Halide-modulated Hollow-Fiber Cu penetration electrode boosts Ampere-Level CO_2 electroreduction to multicarbon products. *Chem. Eng. J.* **2024**, *485*, 150040.

(10) Hao, Q.; Liu, D.-X.; Zhong, H.-X.; Tang, Q.; Yan, J.-M. Electrocatalytic CO_2 reduction in acidic medium. *Chem. Catal.* **2023**, *3* (3), 3.

(11) Li, X.; Wang, Z.; Zhang, J.; Dai, K.; Fan, K.; Dawson, G. Branch-like CdxZn1-xSe/Cu2O@ Cu step-scheme heterojunction for CO_2 photoreduction. *Mater. Today Phys.* **2022**, *26*, 100729.

(12) Liu, M.; Peng, M.; Dong, B.; Teng, Y.; Feng, L.; Xu, Q. Explicating the role of metal centers in porphyrin-based MOFs of PCN-222 (M) for electrochemical reduction of CO_2. *Chin. J. Struct. Chem.* **2022**, *41* (7), 2207046−2207052.

(13) Wan, C.-P.; Yi, J.-D.; Cao, R.; Huang, Y.-B. Conductive Metal/Covalent Organic Frameworks for CO_2 Electro-reduction. *Chin. J. Struct. Chem.* **2022**, *41* (5), 2205001−2205014.

(14) Zhang, Q.; Xu, W.; Xu, J.; Liu, Y.; Zhang, J. High performing and cost-effective metal/metal oxide/metal alloy catalysts/electrodes for low temperature CO_2 electroreduction. *Catal. Today* **2018**, *318*, 15−22.

(15) Fu, H. Q.; Zhang, L.; Zheng, L. R.; Liu, P. F.; Zhao, H.; Yang, H. G. Enhanced CO 2 electroreduction performance over Cl-modified metal catalysts. *J. Mater. Chem. A* **2019**, *7* (20), 12420−12425.

(16) Plana, D.; Flórez-Montano, J.; Celorrio, V.; Pastor, E.; Fermín, D. J. Tuning CO_2 electroreduction efficiency at Pd shells on Au nanocores. *Chem. Commun.* **2013**, *49* (93), 10962−10964.

(17) Cao, L.; Raciti, D.; Li, C.; Livi, K. J.; Rottmann, P. F.; Hemker, K. J.; Mueller, T.; Wang, C. Mechanistic insights for low-overpotential electroreduction of CO_2 to CO on copper nanowires. *ACS Catal.* **2017**, *7* (12), 8578−8587.

(18) Xu, K.; Yang, H.; Hu, Y.; Zhang, F.; Wang, H.; Pan, Y.; Yang, Z.; Zhang, J.; Lin, M.; Dong, Z. Nanowire arrays with abundant Cu−Ni interfaces for electroreduction of CO_2 to ethylene. *Chem. Eng. J.* **2024**, *498*, 155831.

(19) Zhao, Z.; Lu, G. Computational screening of near-surface alloys for CO_2 electroreduction. *ACS Catal.* **2018**, *8* (5), 3885−3894.

(20) Gálvez-Vázquez, M. D. J.; Moreno-García, P.; Guo, H.; Hou, Y.; Dutta, A.; Waldvogel, S. R.; Broekmann, P. Leaded Bronze Alloy as a Catalyst for the Electroreduction of CO_2. *ChemElectrochem* **2019**, *6* (8), 2324−2330.

(21) Yan, J.; Guan, Y.; Marchetti, B.; Liu, Y.; Ning, F.; Yi, J.; Zhou, X.-D. Bi-Eu bimetallic catalysts enabling ultrastable electroreduction of CO_2 with a∼ 100% formate Faradaic efficiency. *Chem. Eng. J.* **2023**, *467*, 143531.

(22) Li, Y.; Shan, W.; Zachman, M. J.; Wang, M.; Hwang, S.; Tabassum, H.; Yang, J.; Yang, X.; Karakalos, S.; Feng, Z.; Wang, G. Atomically dispersed dual-metal site catalysts for enhanced CO_2 reduction: Mechanistic insight into active site structures. *Angew. Chem.* **2022**, *134* (28), No. e202205632.

(23) Hao, Q.; Zhong, H.-X.; Wang, J.-Z.; Liu, K.-H.; Yan, J.-M.; Ren, Z.-H.; Zhou, N.; Zhao, X.; Zhang, H.; Liu, D.-X.; Liu, X. Nickel dual-atom sites for electrochemical carbon dioxide reduction. *Nat. Synth.* **2022**, *1* (9), 719−728.

(24) Li, Y.; Chen, C.; Cao, R.; Pan, Z.; He, H.; Zhou, K. Dual-atom Ag2/graphene catalyst for efficient electroreduction of CO_2 to CO. *Appl. Catal., B* **2020**, *268*, 118747.

(25) Kuhl, K. P.; Cave, E. R.; Abram, D. N.; Jaramillo, T. F. New insights into the electrochemical reduction of carbon dioxide on metallic copper surfaces. *Energy Environ. Sci.* **2012**, *5* (5), 7050−7059.

(26) Takahashi, I.; Koga, O.; Hoshi, N.; Hori, Y. Electrochemical reduction of CO_2 at copper single crystal Cu (S)-[n (111)×(111)] and Cu (S)-[n (110)×(100)] electrodes. *J. Electroanal. Chem.* **2002**, *533* (1−2), 135−143.

(27) Bai, Z.; Jiang, X. Z.; Luo, K. H. Theoretical exploration on the performance of single and dual-atom Cu catalysts on the CO_2 electroreduction process: A DFT study. *Phys. Chem. Chem. Phys.* **2023**, *25* (35), 23717−23727.

(28) Luo, G.; Jing, Y.; Li, Y. Rational design of dual-metal-site catalysts for electroreduction of carbon dioxide. *J. Mater. Chem. A* **2020**, *8* (31), 15809−15815.

(29) Li, F.; Tang, Q. Understanding trends in the activity and selectivity of bi-atom catalysts for the electrochemical reduction of carbon dioxide. *J. Mater. Chem. A* **2021**, *9* (13), 8761−8771.

(30) Feng, H.; Ding, H.; He, P.; Wang, S.; Li, Z.; Zheng, Z.; Yang, Y.; Wei, M.; Zhang, X. Data-driven design of dual-metal-site catalysts for the electrochemical carbon dioxide reduction reaction. *J. Mater. Chem. A* **2022**, *10* (36), 18803−18811.

(31) Ding, H.; Shi, Y.; Li, Z.; Wang, S.; Liang, Y.; Feng, H.; Deng, Y.; Song, X.; Pu, P.; Zhang, X. Active Learning Accelerating to Screen Dual-Metal-Site Catalysts for Electrochemical Carbon Dioxide Reduction Reaction. *ACS Appl. Mater. Interfaces* **2023**, *15* (10), 12986−12997.

(32) Chen, D.; Chen, Z.; Lu, Z.; Tang, J.; Zhang, X.; Singh, C. V. Computational screening of homo and hetero transition metal dimer

catalysts for reduction of CO_2 to C 2 products with high activity and low limiting potential. *J. Mater. Chem. A* **2020**, *8* (40), 21241−21254.
(33) Kresse, G.; Furthmüller, J. Efficiency of ab-initio total energy calculations for metals and semiconductors using a plane-wave basis set. *Comput. Mater. Sci.* **1996**, *6* (1), 15−50.
(34) Kresse, G.; Hafner, J. Ab initio molecular dynamics for liquid metals. *Phys. Rev. B* **1993**, *47* (1), 558.
(35) Hammer, B.; Hansen, L. B.; Nørskov, J. K. Improved adsorption energetics within density-functional theory using revised Perdew-Burke-Ernzerhof functionals. *Phys. Rev. B* **1999**, *59* (11), 7413.
(36) Blöchl, P. E. Projector augmented-wave method. *Phys. Rev. B* **1994**, *50* (24), 17953.
(37) Grimme, S.; Antony, J.; Ehrlich, S.; Krieg, H. A consistent and accurate ab initio parametrization of density functional dispersion correction (DFT-D) for the 94 elements H-Pu. *J. Chem. Phys.* **2010**, *132* (15), 154104.
(38) Grimme, S.; Ehrlich, S.; Goerigk, L. Effect of the damping function in dispersion corrected density functional theory. *J. Comput. Chem.* **2011**, *32* (7), 1456−1465.
(39) Mathew, K.; Kolluru, V. C.; Mula, S.; Steinmann, S. N.; Hennig, R. G. Implicit self-consistent electrolyte model in plane-wave density-functional theory. *J. Chem. Phys.* **2019**, *151* (23), 234101.
(40) Letchworth-Weaver, K.; Arias, T. Joint density functional theory of the electrode-electrolyte interface: Application to fixed electrode potentials, interfacial capacitances, and potentials of zero charge. *Phys. Rev. B* **2012**, *86* (7), 075140.
(41) Mathew, K.; Sundararaman, R.; Letchworth-Weaver, K.; Arias, T. A.; Hennig, R. G. Implicit solvation model for density-functional study of nanocrystal surfaces and reaction pathways. *J. Chem. Phys.* **2014**, *140* (8), 084106.
(42) Garza, A. J.; Bell, A. T.; Head-Gordon, M. Mechanism of CO2 reduction at copper surfaces: Pathways to C_2 products. *ACS Catal.* **2018**, *8* (2), 1490−1499.
(43) Nørskov, J. K.; Rossmeisl, J.; Logadottir, A.; Lindqvist, L.; Kitchin, J. R.; Bligaard, T.; Jonsson, H. Origin of the overpotential for oxygen reduction at a fuel-cell cathode. *J. Phys. Chem. B* **2004**, *108* (46), 17886−17892.
(44) Peterson, A. A.; Abild-Pedersen, F.; Studt, F.; Rossmeisl, J.; Nørskov, J. K. How copper catalyzes the electroreduction of carbon dioxide into hydrocarbon fuels. *Energy Environ. Sci.* **2010**, *3* (9), 1311−1315.
(45) Henkelman, G.; Uberuaga, B. P.; Jónsson, H. A climbing image nudged elastic band method for finding saddle points and minimum energy paths. *J. Chem. Phys.* **2000**, *113* (22), 9901−9904.
(46) Wang, V.; Xu, N.; Liu, J.-C.; Tang, G.; Geng, W.-T. VASPKIT: A user-friendly interface facilitating high-throughput computing and analysis using VASP code. *Comput. Phys. Commun.* **2021**, *267*, 108033.
(47) Yi, W.; Tang, G.; Chen, X.; Yang, B.; Liu, X. qvasp: A flexible toolkit for VASP users in materials simulations. *Comput. Phys. Commun* **2020**, *257*, 107535.
(48) Maintz, S.; Deringer, V. L.; Tchougréeff, A. L.; Dronskowski, R. LOBSTER: A tool to extract chemical bonding from plane-wave based DFT. *J. Comput. Chem.* **2016**, *37* (11), 1030−1035.
(49) Zhu, S.; Wan, K.; Wang, H.; Guo, L.-J.; Shi, X. The role of supported dual-atom on graphitic carbon nitride for selective and efficient CO2 electrochemical reduction. *Nanotechnology* **2021**, *32* (38), 385404.
(50) Guo, C.; Zhang, T.; Deng, X.; Liang, X.; Guo, W.; Lu, X.; Wu, C. M. L. Electrochemical CO_2 reduction to C_1 products on single nickel/cobalt/iron-doped graphitic carbon nitride: A DFT study. *ChemSuschem* **2019**, *12* (23), 5126−5132.
(51) Back, S.; Jung, Y. TiC-and TiN-supported single-atom catalysts for dramatic improvements in CO_2 electrochemical reduction to CH_4. *ACS Energy Lett.* **2017**, *2* (5), 969−975.
(52) Montoya, J. H.; Tsai, C.; Vojvodic, A.; Nørskov, J. K. The challenge of electrochemical ammonia synthesis: A new perspective on the role of nitrogen scaling relations. *ChemSuschem* **2015**, *8* (13), 2180−2186.
(53) Zou, W.; Lu, R.; Liu, X.; Xiao, G.; Liao, X.; Wang, Z.; Zhao, Y. Theoretical insights into dual-atom catalysts for the oxygen reduction reaction: The crucial role of orbital polarization. *J. Mater. Chem. A* **2022**, *10* (16), 9150−9160.
(54) Hu, R.; Li, Y.; Zeng, Q.; Shang, J. Role of active sites in N-coordinated Fe-Co dual-metal doped graphene for oxygen reduction and evolution reactions: A theoretical insight. *Appl. Surf. Sci.* **2020**, *525*, 146588.
(55) Montoya, J. H.; Shi, C.; Chan, K.; Nørskov, J. K. Theoretical insights into a CO dimerization mechanism in CO2 electroreduction. *J. Phys. Chem. Lett.* **2015**, *6* (11), 2032−2037.
(56) Kibria, M. G.; Edwards, J. P.; Gabardo, C. M.; Dinh, C.-T.; Seifitokaldani, A.; Sinton, D.; Sargent, E. H. Electrochemical CO_2 reduction into chemical feedstocks: From mechanistic electrocatalysis models to system design. *Adv. Mater.* **2019**, *31* (31), 1807166.
(57) Peterson, A. A.; Nørskov, J. K. Activity descriptors for CO_2 electroreduction to methane on transition-metal catalysts. *J. Phys. Chem. Lett.* **2012**, *3* (2), 251−258.
(58) Liu, X.; Xiao, J.; Peng, H.; Hong, X.; Chan, K.; Nørskov, J. K. Understanding trends in electrochemical carbon dioxide reduction rates. *Nat. Commun.* **2017**, *8* (1), 15438.
(59) Chen, A.; Zhang, X.; Chen, L.; Yao, S.; Zhou, Z. A machine learning model on simple features for CO_2 reduction electrocatalysts. *J. Phys. Chem. C* **2020**, *124* (41), 22471−22478.
(60) Xu, S.; Carter, E. A. Theoretical insights into heterogeneous (photo) electrochemical CO_2 reduction. *Chem. Rev.* **2019**, *119* (11), 6631−6669.
(61) Wei, X.; Wei, S.; Cao, S.; Hu, Y.; Zhou, S.; Liu, S.; Wang, Z.; Lu, X. Cu acting as Fe activity promoter in dual-atom Cu/Fe-NC catalyst in CO_2RR to C_1 products. *Appl. Surf. Sci.* **2021**, *564*, 150423.
(62) Liu, J. H.; Yang, L. M.; Ganz, E. Two-Dimensional Organometallic TM3−C12S12 Monolayers for Electrocatalytic Reduction of CO_2. *Energy Environ. Mater.* **2019**, *2* (3), 193−200.
(63) Wang, S.; Ma, W.; Sang, Z.; Hou, F.; Si, W.; Guo, J.; Liang, J.; Yang, D. Dual-modification of manganese oxide by heterostructure and cation pre-intercalation for high-rate and stable zinc-ion storage. *J. Energy Chem.* **2022**, *67*, 82−91.
(64) Liu, S.; Zhang, B.; Zhang, L.; Sun, J. Rational design strategies of Cu-based electrocatalysts for CO2 electroreduction to C_2 products. *J. Energy Chem.* **2022**, *71*, 63−82.
(65) Zhao, K.; Nie, X.; Wang, H.; Chen, S.; Quan, X.; Yu, H.; Choi, W.; Zhang, G.; Kim, B.; Chen, J. G. Selective electroreduction of CO_2 to acetone by single copper atoms anchored on N-doped porous carbon. *Nat. Commun.* **2020**, *11* (1), 2455.
(66) Li, H.; Wu, D.; Wu, J.; Song, Y.; Lv, W.; Duan, Z.; Ma, D. Mechanistic understanding of the electrocatalytic conversion of CO into C_2+ products by double-atom catalysts. *Mater. Today Phys.* **2023**, *37*, 101203.
(67) Ma, X.; Xu, L.; Liu, S.; Zhang, L.; Tan, X.; Wu, L.; Feng, J.; Liu, Z.; Sun, X.; Han, B. Electrochemical CC coupling between CO_2 and formaldehyde into ethanol. *Chem. Catal.* **2022**, *2* (11), 3207−3224.

https://doi.org/10.1021/acs.iecr.4c04831
Ind. Eng. Chem. Res. 2025, 64, 4378−4387